Received: August 22, 2020 Revised: November 5, 2020 Accepted: November 23, 2020

(onlinelibrary.wiley.com) DOI: 10.1111/ner.13338

Neurocapillary-Modulation

Niranjan Khadka, PhD[1]; Marom Bikson, PhD[2]

ABSTRACT

Objectives: We consider two consequences of brain capillary ultrastructure in neuromodulation. First, blood-brain barrier (BBB) polarization as a consequence of current crossing between interstitial space and the blood. Second, interstitial current flow distortion around capillaries impacting neuronal stimulation.

Materials and Methods: We developed computational models of BBB ultrastructure morphologies to first assess electric field amplification at the BBB (principle 1) and neuron polarization amplification by the presence of capillaries (principle 2). We adapt neuron cable theory to develop an analytical solution for maximum BBB polarization sensitivity.

Results: Electrical current crosses between the brain parenchyma (interstitial space) and capillaries, producing BBB electric fields (E_{BBB}) that are >400x of the average parenchyma electric field ($\bar{E}_{BRAIN}$), which in turn modulates transport across the BBB. Specifically, for a BBB space constant (λ_{BBB}) and wall thickness ($d_{th\text{-}BBB}$), the analytical solution for maximal BBB electric field (E^{A}_{BBB}) is given as: $(\bar{E}_{BRAIN} \times \lambda_{BBB})/d_{th\text{-}BBB}$. Electrical current in the brain parenchyma is distorted around brain capillaries, amplifying neuronal polarization. Specifically, capillary ultrastructure produces ~50% modulation of the $\bar{E}_{BRAIN}$ over the ~40 μm inter-capillary distance. The divergence of E_{BRAIN} (Activating function) is thus ~100 kV/m^2 per unit $\bar{E}_{BRAIN}$.

Conclusions: BBB stimulation by principle 1 suggests novel therapeutic strategies such as boosting metabolic capacity or interstitial fluid clearance. Whereas the spatial profile of E_{BRAIN} is traditionally assumed to depend only on macroscopic anatomy, principle 2 suggest a central role for local capillary ultrastructure—which impact forms of neuromodulation including deep brain stimulation (DBS), spinal cord stimulation (SCS), transcranial magnetic stimulation (TMS), electroconvulsive therapy (ECT), and transcranial electrical stimulation (tES)/transcranial direct current stimulation (tDCS).

Keywords: Blood-brain Barrier, BBB amplification, electric field, neurovascular coupling, neurovascular unit, neuron polarization

Conflict of Interest: The City University of New York (CUNY) has IP on neuro-stimulation systems and methods with authors Niranjan Khadka and Marom Bikson as inventors. Marom Bikson has equity in Soterix Medical. Marom Bikson served on the advisory boards, received grants, and/or consulted for Boston Scientific, Mecta, Halo Neuroscience, and GlaxoSmithKline Inc. Dr. Khadka has no conflicts of interest to disclose.

INTRODUCTION

Vascular responses are ubiquitous across neuromodulation (1–6) but are considered epiphenomena to neuronal stimulation. Common functional imaging techniques measure hemodynamic response (e.g., Arterial Spin Labeling fMRI, H_20^{15} PET, SPECT, BOLD fMRI, fNIRS) are interpreted as indexing neuronal activation through neurovascular coupling (NVC). NVC is the mechanism by which increased neuronal activity regulates cerebral blood flow (CBF) to assure that the blood supply of the brain is commensurate to local cellular metabolism (7, 8). The mechanisms of NVC are studied to enhance interpretation of hemodynamic-based imaging techniques (9) and understand the role of cerebral blood flow and in disease such as hypertension, Alzheimer disease, and stroke (7). NVC is activated in animals using mechanosensory stimulation (9–11), visual stimulation (12–14), and electrical stimulation of peripheral (15, 16) or central axons *distal* to the brain region of interest (17–19). Stimulation applied directly to a brain region is a special case where brain vasculature can be directly activated (20–23) which 1) reverses the typical recruitment order of NVC, suggesting functional imaging in fact shows direct hemodynamic activation and 2) resulting in peculiar (supra-physiological) neurovascular changes that suggest novel therapeutic strategies (e.g., metabolic capacity, interstitial clearance).

The brain capillary bed is a dense network of interconnected vessels formed by specialized endothelial cells. The blood-brain barrier (BBB) is the interface between the blood and brain interstitial fluid. Endothelial cells are sealed together by tight junctions, resulting in an exceptionally resistive BBB. Capillary diameter in

Address correspondence to: Marom Bikson, PhD, Department of Biomedical Engineering, The City College of New York, CUNY, New York, NY, USA. Email: bikson@ccny.cuny.edu; Niranjan Khadka, PhD, Department of Psychiatry, Laboratory for Neuropsychiatry and Neuromodulation, Massachusetts General Hospital, Harvard Medical School, MA, USA. Email: nironzan@gmail.com

[1] Department of Psychiatry, Laboratory for Neuropsychiatry and Neuromodulation, Massachusetts General Hospital, Harvard Medical School, Boston, MA, USA; and
[2] Department of Biomedical Engineering, The City College of New York, CUNY, New York, NY, USA

For more information on author guidelines, an explanation of our peer review process, and conflict of interest informed consent policies, please go to http://www.wiley.com/WileyCDA/Section/id-301854.html

Source(s) of financial support: This study was partially funded by grants to MB from NIH (NIMH 1R01MH111896, NINDS 1R01NS101362, NCI U54CA137788/U54CA132378, R03 NS054783, 1R01NS112996-01A1) New York State Department of Health (NYS DOH, DOH01-C31291GG), and cycle 50 PSC-CUNY.

the brain is ~10 μm and the average intercapillary distance is ~40 μm (24, 25), such that neuronal processes are <20 μm from the nearest capillary (26). Moreover, brain capillaries are encased in extracellular matrix proteins and surrounded by specialized neuronal processes and the perivascular end feet of astrocytic glia (27).

Here, we consider two consequences of BBB ultrastructure in neuromodulation. First, to what extent does the BBB polarizes as a consequence of current crossing between interstitial space and the blood (principle 1). NVC and interstitial fluid clearance govern brain health and can be compromised in disease (7). For example, Alzheimer's disease (AD) is associated with build-up of misfolded proteins (28, 29) and impaired clearance systems (30). Generally, NVC and interstitial fluid clearance is compromised with age (31–33), which may further be linked to the role of clearance mechanisms during sleep (34). Interventions enhancing clearance in the brain may treat diverse neurological disorders including of aging (29, 35). By predicting BBB polarization, principle 2 provides a substrate for developing neurocapillary-modulation targeting brain clearance. For example, we proposed transcranial direct current stimulation (tDCS) boosts interstitial fluid transport based on BBB electro-osmosis (21).

Second, current flow through the interstitial space is considered insensitive to cellular ultrastructure (36), which has importance consequences in predicting which neuronal elements are stimulated (37). But, the role of capillaries in distorting current flow is addressed for the first time here (principle 2). We specifically advance the theory that if microscopic electric field gradients (activating function) around neurons created by BBB ultrastructure is larger than that produced by macroscopic tissues changes (38–41), then neuronal stimulation is in fact predicted by the average local electric field (42, 43) as convoluted by regional BBB properties. The consequences of this analysis span all forms of brain stimulation including deep brain stimulation (DBS), spinal cord stimulation (SCS), transcranial magnetic stimulation (TMS), electroconvulsive therapy (ECT), and transcranial electrical stimulation techniques (tES) such a tDCS.

MATERIALS AND METHODS

The anatomy of brain vasculature is intractably complex across scales, and current crossing the BBB can exits at neighboring locations or traverse broadly across vascular system, such that macroscopic anatomy may impact microscopic current flow. We overcome this by designing models (e.g., capillary orientation and capillary border boundary conditions) such that assessed variables (e.g., question being asked) were independent of exterior volume dimensions or capillary length. For electric field amplification at the BBB, the models address question regarding the maximum current density crossing the BBB for a given capillary morphology. We also adapt neuron cable theory (44–48) to develop an analytical solution for maximum BBB polarization sensitivity. For addressing neuron polarization amplification by capillary ultrastructure, parallel vessels (with no tortuosity and region-specific inter-capillary distance) are a conservative model.

Model Construction and Solution Method

We developed a computer-aided design (CAD) model of BBB ultrastructure to first assess electric field amplification at the BBB (principle 1) and neuron polarization amplification by capillaries (principle 2). Different prototypical capillaries morphologies were modeled as CAD files in SolidWorks (Dassault Systemes Corp., MA, USA) and imported into Simpleware (Synopsys Inc., CA, USA) to generate an adaptive tetrahedral mesh using a built-in voxel-based meshing algorithm. Mesh density was refined until additional model refinement produced less than 1% difference in extracellular voltage at the BBB. The resulting model consisted of >28 million, > 68 million, and >41 tetrahedral elements for the three exemplary prototypical capillary morphologies: (morphology 1) semi-circular loop (fixed curvature width) with semi-infinite orthogonal straight segments (Fig. 1a1); (morphology 2) semi-circular loop (varied curvatures) with semi-infinite parallel straight segments (Fig. 1b1); (morphology 3) semi-infinite straight tube with variant terminal conditions (Fig. 1c1), and > 38 million, > 29 million, > 45 million, > 68 million, and > 70 million for cortical (Fig. 2a1), white matter (Fig. 2a2), subcortical (Fig. 2a3), thoracic white matter (Fig. 2a4), and thoracic gray matter (Fig. 2a5) vasculature models, respectively.

Normal current density was applied to the one surface of the brain voxel while the opposite surface of the brain voxel was grounded, with the remaining external boundaries insulated. For computation, we used 0.08 A/m^2 (corresponding to ~1 mA tDCS (42)); however, all results were reported as normalized (i.e., per unit parenchyma electric field) by dividing results by the average ("bulk") parenchyma electric field ($\bar{E}_{BRAIN}$). This is the same as the uniform electric field produced in a model with homogenous resistivity (i.e., only brain parenchyma). Laplace equation ($\nabla\cdot(\sigma\nabla V) = 0$, where V is extracellular voltage and σ is electrical conductivity) was applied and solved as the field equation to determine the extracellular voltage distribution throughout the model. Three-dimensional (3D) extracellular voltage, electric field, and activating function were predicted in different capillary morphologies, and resulting BBB polarization length, BBB amplification factor, or neuronal polarization amplification by capillary ultrastructure were calculated.

Models of BBB Electric Field Amplification (Principle 1): Numerical Solutions

For electric field amplification at the BBB, we simulated three variations of capillary morphology 1, namely I, I_1, and I_2, with fixed curvature width (1000 μm), and varied wall thickness ($d_{th\text{-}BBB}$), lumen diameter (d_l) and brain voxel volume. In variation I, the $d_{th\text{-}BBB}$ was 10 μm, d_l was 100 μm, and brain voxel volume was 2.2×10^{12} μm^3. In variation I_1 and I_2, the $d_{th\text{-}BBB}$ was 1 μm and d_l was 10 μm, while the brain voxel volumes were 5.1×10^7 μm^3 and 1.1×10^8 μm^3, respectively. Unless otherwise mentioned, 2.2×10^{12} μm^3 was used as a standard brain voxel volume for the remaining capillary morphology models. Capillary morphology 2 included two morphological variations, namely II and II_2. In both of these variations, the $d_{th\text{-}BBB}$ was 10 μm and d_l was 100 μm, whereas the curvature widths were 1000 μm and 200 μm, respectively, for variation II and II_2. Capillary morphology 3 included III and III_1 morphological variations with variant terminal conditions. In variation III, one terminal of a semi-infinite straight tube was open, whereas both terminals were sealed in variation III_1. The $d_{th\text{-}BBB}$ was 10 μm and d_l was 100 μm for both III and III_1 variations. The semi-circular loop of capillary morphology 1 and 2 or tapered end of capillary morphology 3 was oriented toward the energized surface the brain voxel. Capillary wall and lumen dimensions were based on cadaveric studies and imaging data (49–56).

Unless otherwise indicated, standard electrical resistivity (reciprocal of electrical conductivity) was assigned to each model domain as: capillary wall: 1×10^5 Ω.m; capillary lumen: 1.42 Ω.m; and brain parenchyma: 3.62 Ω.m. In some simulations, capillary wall resistivity was increased or decreased 100-fold.

Capillary morphology 1 was positioned at the middle of the brain voxel in such a way that boundaries of capillary wall and lumen at the terminating ends of the orthogonal straight segments were sealed. Capillary wall and lumen boundaries at the terminating ends of the semi-infinite parallel segments of capillary morphology 2 were

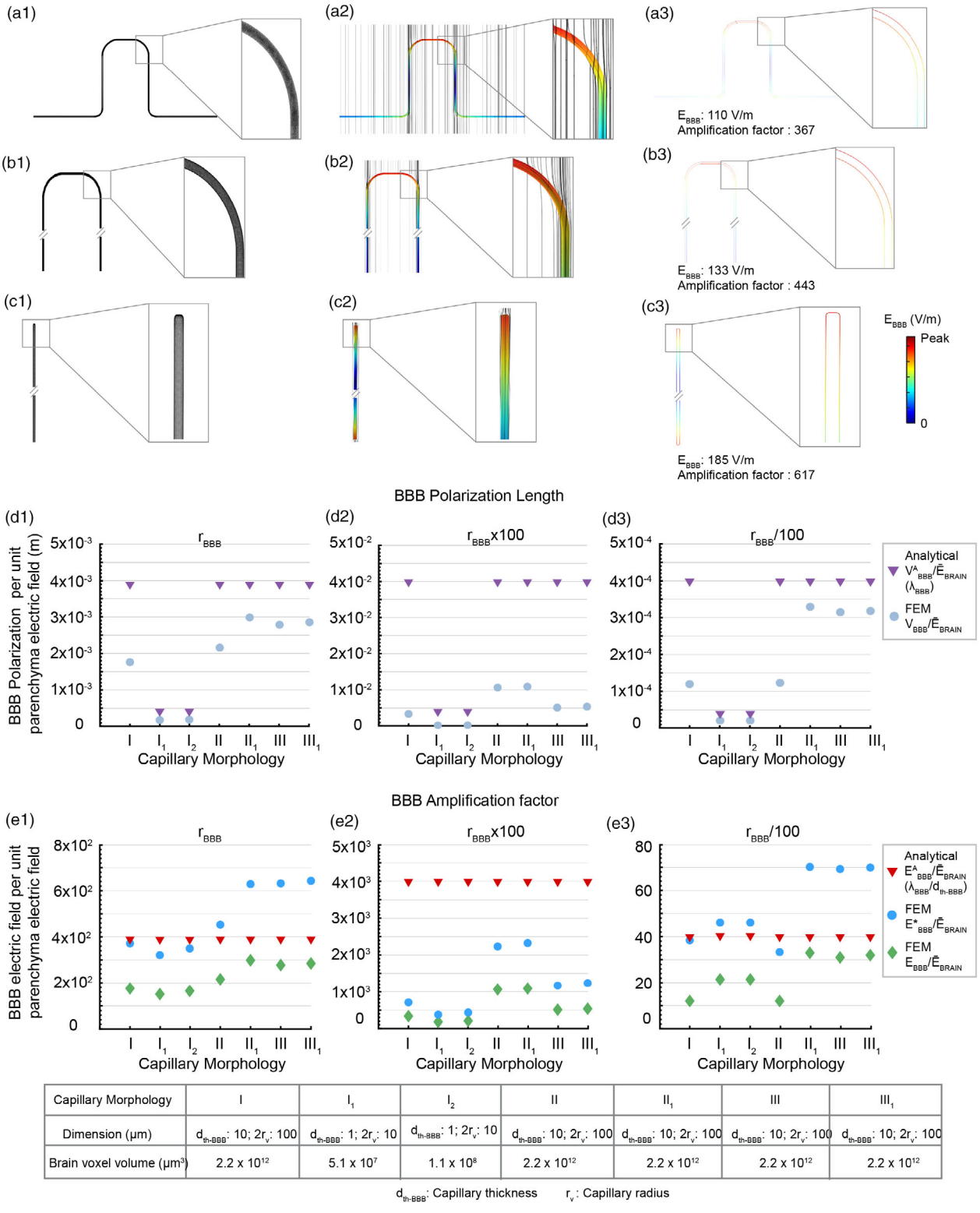

Capillary Morphology	I	I_1	I_2	II	II_1	III	III_1
Dimension (μm)	$d_{th\text{-}BBB}$: 10; $2r_v$: 100	$d_{th\text{-}BBB}$: 1; $2r_v$: 10	$d_{th\text{-}BBB}$: 1; $2r_v$: 10	$d_{th\text{-}BBB}$: 10; $2r_v$: 100	$d_{th\text{-}BBB}$: 10; $2r_v$: 100	$d_{th\text{-}BBB}$: 10; $2r_v$: 100	$d_{th\text{-}BBB}$: 10; $2r_v$: 100
Brain voxel volume (μm^3)	2.2×10^{12}	5.1×10^{7}	1.1×10^{8}	2.2×10^{12}	2.2×10^{12}	2.2×10^{12}	2.2×10^{12}

$d_{th\text{-}BBB}$: Capillary thickness r_v: Capillary radius

Figure 1. Legend on next page.

open (ground). Capillary morphology 3 was also positioned at the middle of the brain voxel, and the capillary lumen domain was enclosed by the capillary wall domain, with 1 μm spacing between them. Together they formed a semi-infinite membrane.

The numerical maxima for BBB polarization length (BBB polarization per unit parenchyma electric field) is given as:

$$V_{BBB}/\bar{E}_{BRAIN} \quad (1)$$

where V_{BBB} is a predicted BBB polarization (V) and $\bar{E}_{BRAIN}$ is an average predicted parenchyma electric field (V/m). The numerically computed average BBB electric field amplification (BBB electric field per unit parenchyma electric field) is expressed as:

$$E_{BBB}/\bar{E}_{BRAIN} \quad (2)$$

where E_{BBB} (V/m) is an average electric field across the capillary wall thickness, calculated as V_{BBB} per BBB thickness:

$$V_{BBB}/d_{th-BBB} \quad (3)$$

The punctate (maximal) BBB electric field amplification is expressed as:

$$E^*_{BBB}/\bar{E}_{BRAIN} \quad (4)$$

where E^*_{BBB} (V/m) is the maximum predicted BBB electric field within the capillary wall, noting the electric field inside the capillary wall can change across the wall depth.

Models of BBB Electric Field Amplification (Principle 1): Analytical Solutions

Analytical analysis of polarization of axon terminals in an electric field based on cable theory (47, 48, 57) shows the maximal polarization that can be experienced at a bent or terminating axon terminal as:

$$V_{TM} = EF \times \lambda_m \quad (5)$$

where V_{TM} is the change in axon terminal transmembrane potential, EF is the electric field around the terminal (V/m), and λ_m is the terminal space constant (m). λ_m is a function of only the axon membrane resistivity (r_m:Ω.m) and axon intracellular resistivity (r_i:Ω.m) as:

$$\lambda_m = (r_m/r_i)^{1/2} \quad (6)$$

This maximal axon terminal polarization sensitivity may be secondarily amplified by "active" sub-threshold active channels at the terminal (58) and trigger a supra-threshold action potential. A maximal "passive" neuronal sensitivity of λ_m still applies, including to more complex neuronal structures (44, 59).

Our analytical model for BBB polarization adapts this same cable theory where we model the capillary wall (BBB) as analogous to a continuous extracellular membrane and we model the capillary lumen (blood) as analogous to the continuous intracellular compartment. The analytically derived maximal BBB polarization is therefore expressed as:

$$V^A_{BBB} = \bar{E}_{BRAIN} \times \lambda_{BBB} \quad (7)$$

where V^A_{BBB} is BBB polarization (V), $\bar{E}_{BRAIN}$ is an average parenchyma electric field (V/m), and λ_{BBB} is defined here as the BBB space constant (m). λ_{BBB} is a function of only the capillary wall (BBB) resistivity (r_{BBB}: Ω.m) and capillary lumen (blood) resistivity (r_{BLOOD}: Ω.m) as:

$$\lambda_{BBB} = (r_{BBB}/r_{BLOOD})^{1/2} \quad (8)$$

The analytical polarization length (V^A_{BBB} per unit $\bar{E}_{BRAIN}$) is thus λ_{BBB}. The maximal analytical BBB electric field is then expressed as:

$$E^A_{BBB} = V^A_{BBB}/d_{th-BBB} \quad (9)$$

The analytical maximal amplification factor (E^A_{BBB} per unit $\bar{E}_{BRAIN}$) is then estimated as:

$$\lambda_{BBB}/d_{th-BBB} \quad (10)$$

Brain vasculature structure and properties are not simply analogous to axons of neurons, so we use numerical FEM simulations of various exemplary capillary morphologies to test whether our analytical solution predicts maximal BBB polarization and so also the maximal BBB electric field. While we designed the models such that the V_{BBB} and E_{BBB} were independent of brain voxel size, anomalous current patterns where blood vessel contacting model boundaries were not considered.

Models of Neuron Polarization Amplification (Principle 2)

For neuron polarization amplification by capillaries, we modeled semi-infinite parallel solid capillaries, adjusting the length density (L_v) of capillaries for varied brain regions (cortical

Figure 1. Maximal BBB polarization and electric field amplification across prototypical capillary morphologies compared to analytical maxima. Architecture of three exemplary capillary morphologies (a1) capillary morphology 1: semi-circular loop (fixed curvature width) with semi-infinite orthogonal straight segments, (b1) capillary morphology 2: semi-circular loop (varied curvatures) with semi-infinite parallel straight segments, and (c1) capillary morphology 3: semi-infinite straight tube with tapered end. $d_{th\text{-}BBB}$ and $2r_v$ refers to capillary wall thickness and capillary lumen diameter, respectively. Current flow and specifically maximal electric field intensity across the BBB (E_{BBB}) were predicted. Capillary morphology 1 include three morphological variations (I, I_1, and I_2) with fixed curvature width, but varied $d_{th\text{-}BBB}$ (I: 10 μm; I_1: 1 μm; I_2: 1 μm) and $2r_v$ (I: 100 μm; I_1: 10 μm; I_2: 10 μm). Capillary morphology 2 includes two morphological variations (II and II_1) with similar $d_{th\text{-}BBB}$ (10 μm), $2r_v$ (100 μm) but varied curvature width (II: 1000 μm; II_1: 200 μm). Capillary morphology 3 includes two morphological variations (III and III_1) with similar $d_{th\text{-}BBB}$ (10 μm), $2r_v$ (100 μm) but varied terminal conditions (III: one end open; III_1: both ends sealed). Predicted brain current flow pattern (black flux lines) and BBB electric field (false color) are showed for capillary morphology 1, parameters I (a2, a3), capillary morphology 2, parameters II (b2, b3), and capillary morphology 3, parameters III (c2, c3). The amplification factor (maximal E_{BBB} per unit parenchyma electric field) was 367, 443, and 617, respectively, for these three exemplary BBB capillary morphologies and parameters (a3; b3; c3). In addition, for each capillary morphology and variation, BBB resistivity (and so BBB space constant) was varied from a standard value (d1, e1; $r_{BBB} = 1 \times 10^5$ Ω.m) by a factor of 100 up (d2; e2; $r_{BBB} \times 100 = 1 \times 10^7$ Ω.m) or down (d3; e3; $r_{BBB}/100 = 1 \times 10^3$ Ω.m). For each FEM simulation, BBB polarization per unit brain parenchyma (BBB polarization length) and E_{BBB} per unit brain parenchyma (BBB Amplification factor) is summarized. Since E_{BBB} was not uniform across the capillary wall, we report "punctate" E^*_{BBB} (at any point within the capillary wall) as well as the average E_{BBB} ($V_{BBB}/d_{th\text{-}BBB}$). Finally, the analytically derived (see Methods) maximum BBB polarization length (λ_{BBB}) and BBB amplification factor ($\lambda_{BBB}/d_{th\text{-}BBB}$) are reported for each model. [Color figure can be viewed at wileyonlinelibrary.com]

gray-matter, white-matter, subcortical, thoracic white-matter, and thoracic gray-matter; Fig. 2) that are therapeutic targets (Table 1) for different modes of electrical stimulation (tDCS, TMS, ECT, DBS, and SCS). Solid capillaries were modeled with a uniform resistivity of 1×10^5 Ω.m.

Factors driving neuron polarization amplification by capillaries were quantified as normalized electric fields (per unit parenchyma electric field) and normalized activating functions (per unit parenchyma electric field) at three different brain voxel locations: proximal (~5 μm away from capillary), middle (in between two capillaries), and distal (no capillary zone) (Fig. 2b1–b5).

Exemplary Translational Applications (Principle 2) Across Neuromodulation Modalities

We simulated three modalities of neuromodulation: tES, SCS, and DBS to demonstrate the modulation of electric field and thus the neuronal polarization by the capillary ultrastructure. The modeling approach is multiscale. In the first step, we computed brain current flow based on electrode position and macroscopic tissues properties—without capillaries represented. In the second setup, in selected ROI, we compute how the incident current is modulated by region-specific capillary structure. Specifically, the electric field and activating function for each standard macroscopic models (without capillaries) were sampled from two

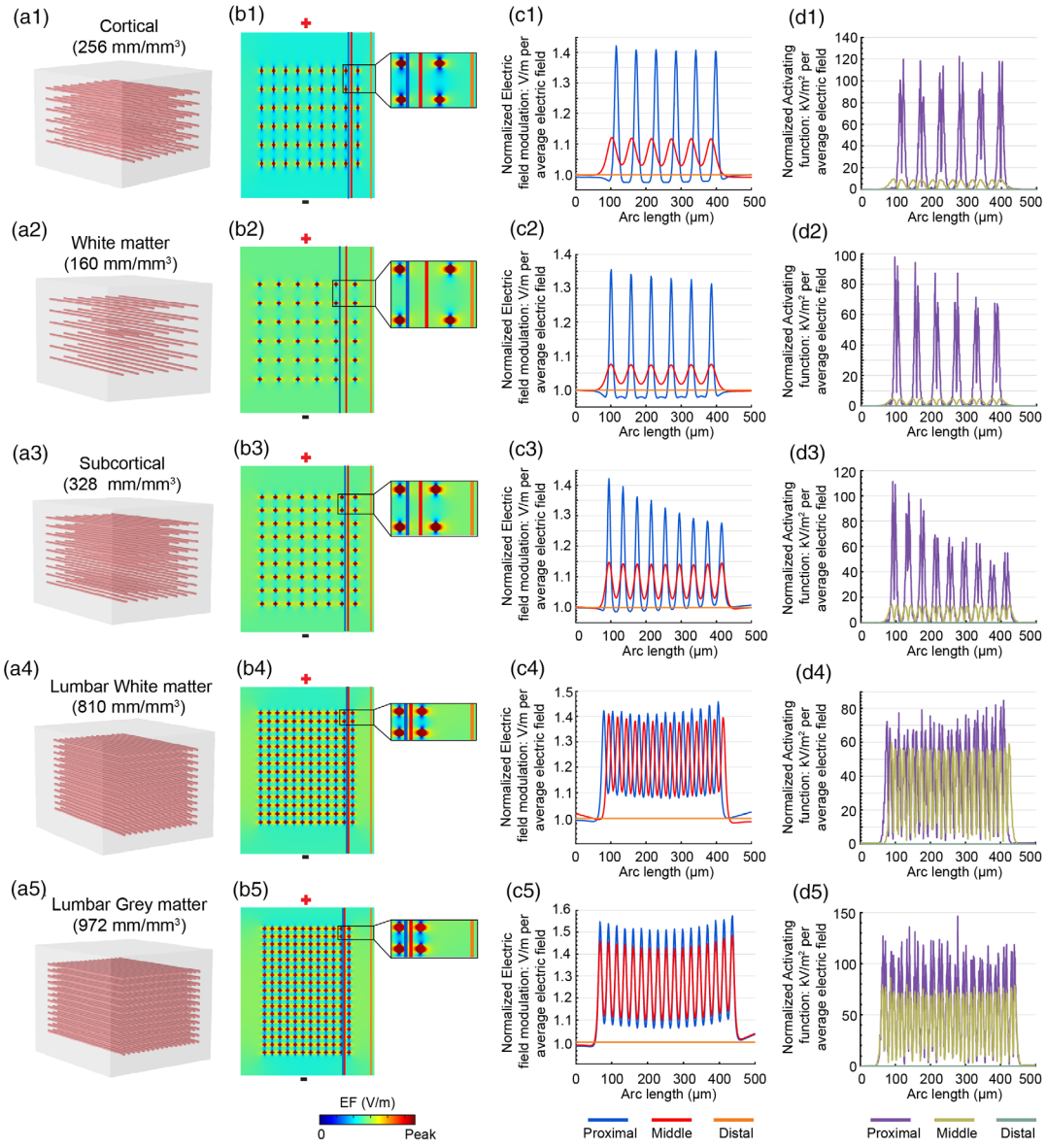

Figure 2. Impact of capillary ultrastructure on brain electric field. We consider capillary ultrastructure network for five brain regions (cortical, white-matter, subcortical, thoracic white-matter, and thoracic gray-matter). a1–a5. Illustrates capillary network for these brain regions, noting the regional capillary length density (mm length per mm^3 volume). b1–b5. Predicted electric field in a plane crossing the capillary bed, shows local distortion of electric field by the capillaries. Also illustrated is the straight trajectory for sampling of electric field and activating function: 1) proximal trajectory (~5 μm away from nearest capillary; blue line), middle trajectory (in between adjacent capillaries; red line), and distal trajectory (region without capillary; orange line). c1–c5. Normalized electric field magnitude (per unit parenchyma electric field) along three trajectories. The degree of electric field modulation was higher for trajectories passing nearer capillaries and for denser capillary beds. d1–d5. Electric field gradient (activating function) magnitude (per unit parenchyma electric field) along three trajectories. Neuronal activation at the proximity of a capillary was ~100 kV/m^2 per unit average parenchyma electric field ($\hat{E}_{BRAIN}$). Activating functions were higher for trajectories passing nearer capillaries and for denser capillary beds. [Color figure can be viewed at wileyonlinelibrary.com]

3 mm × 3 mm ROIs (solid black and dotted black, see Fig. 3), defined in the respective brain/spinal cord region (tES: gray matter [GM] and white matter [WM]; SCS: dorsal column [DC] and dorsal horn [DH]; DBS: subthalamic nucleus [STN] and globus pallidus internus [GPi]). Then the average electric field within the ROIs from the standard models were applied to a brain voxel including the vascular-ultrastructure model (with brain/spinal cord specific capillary density), and the corresponding modulated electric fields and activating functions were predicted.

For the tES modality (tDCS in this case), we simulated a M1-SO montage (anode over M1) with 5 × 5 cm^2 sponge electrode and applied 1 mA via the anode, while the cathode was grounded. The respective tissue conductivities, model construction, and the computational solution method were discussed in detail elsewhere (74–76). For the SCS model, we simulated a T8–T12 SCS model with an eight-contact SCS lead (C1–C8; C1 is the deeper contact) positioned epidurally and energized the C3 (anode: 5 mA_{peak}), and C5 (cathode) contacts. We elsewhere discussed the modeling approaches in detail (72, 77, 78). In the DBS modality, a four-contact DBS lead (C0–C3; C0 is the deeper contact) was positioned into the STN and the contacts were energized using a bipolar electrode configuration (C2: anode [5 mA_{peak}] and C3: cathode). The model construction and solution methods were discussed in detail elsewhere (68).

RESULTS

Theoretical Basis for Maximum Electric Field Amplification at the BBB (Principle 1)

To develop a theory quantifying BBB (capillary wall) polarization, resulting from current flow between the brain parenchyma and the blood during neuromodulation, we modeled stimulation across capillary segments of varied morphologies that are intended to capture maximum local polarization across a complex capillary network. We considered three prototypical capillary morphologies (Fig. 1a1, b1, c1). Capillary morphology 1 was a semi-circular loop (fixed curvature width) with semi-infinite orthogonal straight segments, with variants of capillary size (I, I_1, and I_2). Capillary morphology 2 was a semi-circular loop (varied curvatures) with semi-infinite parallel straight segments with variants of loop curvature (II and II_1). Capillary morphology 3 was a semi-infinite straight tube with two variants of terminal conditions (III, III_1). FEM simulation predicted current flow though the brain voxel containing the capillary (Fig. 1a2,b2,c2), and specifically current flow across the BBB (Fig. 1a3,b3,c3). Models were designed so that maximum polarization was insensitive to the modeled tissue boundary size (see Methods).

For each morphology, the maximum voltage across the BBB (V_{BBB}) and electric field across the BBB (E_{BBB}) are reported as normalized to unit parenchyma electric field (E_{BRAIN}). This allows reporting of BBB polarization length (V_{BBB} per unit E_{BRAIN}; Fig. 1, row d) and the BBB amplification factor (E_{BBB} per unit E_{BRAIN}; Fig. 1, row e). Thus, for any specific neuromodulation technology with a given average electric field in a brain target, the resulting BBB electric field is this average electric field times the region-specific amplification factor. Finally, for each capillary morphology, BBB resistivity was varied from a standard value (r_{BBB}: Fig. 1d1,e1) up or down by a factor of 100 (r_{BBB} × 100: Fig. 1d2,e2; r_{BBB}/100: Fig. 1d3,e3).

Note that the voltages (V_{BBB}) and electric fields (E_{BBB}) across the BBB segments varied for any capillary morphology; consistent

Table 1. Predicted Maximal V_{BBB} and E_{BBB} for Various Therapeutic Modalities and Brain Targets.

Brain region	Therapy mode	Capillary thickness (m)	r_{BBB}: ρ_{BBB}*$d_{th\text{-}BBB}$/($2\pi r_v$) (Ω.m)	r_{BLOOD}: ρ_{BBB}/($\pi d^2/4$) (Ω.m)	λ_{BBB}: $(r_{BBB}/r_{BLOOD})^{1/2}$ (m) (44–46)	Average electric field in brain ROI $\bar{E}_{BRAIN}$ (V/m)	V^A_{BBB}: $\bar{E}_{BRAIN}$* λ (V)	E^A_{BBB}: $V_{BBB}/d_{th\text{-}BBB}$ (V/m)
Cortical	tDCS	1×10^{-6}	4.92×10^3	6.08×10^3	2.84×10^{-4}	0.3–0.6 (60, 61)	8.53×10^{-5} to 1.71×10^{-4}	85–171
Cortical	TMS	1×10^{-6}	4.92×10^3	6.08×10^3	2.84×10^{-4}	56.5–157.7 (62–64)	1.61×10^{-2} to 4.49×10^{-2}	1.61×10^4–4.49×10^4
Cortical	ECT	1×10^{-6}	4.92×10^3	6.08×10^3	2.84×10^{-4}	125–240 (63, 65, 66)	3.56×10^{-2} to 6.83×10^{-2}	3.56×10^4–6.83×10^4
Subcortical	ECT	1×10^{-6}	4.92×10^3	6.28×10^3	2.82×10^{-4}	100–125 (65, 67)	2.82×10^{-2} to 3.52×10^{-2}	2.82×10^4–3.52×10^4
STN, GPi, Thalamus	DBS	1×10^{-6}	4.99×10^3	6.57×10^3	2.78×10^{-4}	200–1069 (68–71)	5.60×10^{-2} to 2.97×10^{-1}	5.56×10^4–2.97×10^5
White matter	SCS	1×10^{-6}	5.08×10^3	2.70×10^{-4}	2.70×10^{-4}	14.7–25.6 (72, 73)	3.97×10^{-3} to 6.91×10^{-3}	3.97×10^3–6.91×10^3
Gray matter	SCS	1×10^{-6}	5.31×10^3	7.28×10^3	2.70×10^{-4}	42 (72)	1.13×10^{-2} to 1.49×10^{-2}	1.13×10^4–1.49×10^4

Region-specific capillary anatomies and resistivities were used to calculate a representative BBB space constant (λ_{BBB}) for each region. Based on our analytical derivation, maximum voltage across the BBB (V^A_{BBB}) and electric field across the BBB (E^A_{BBB}) are calculated.

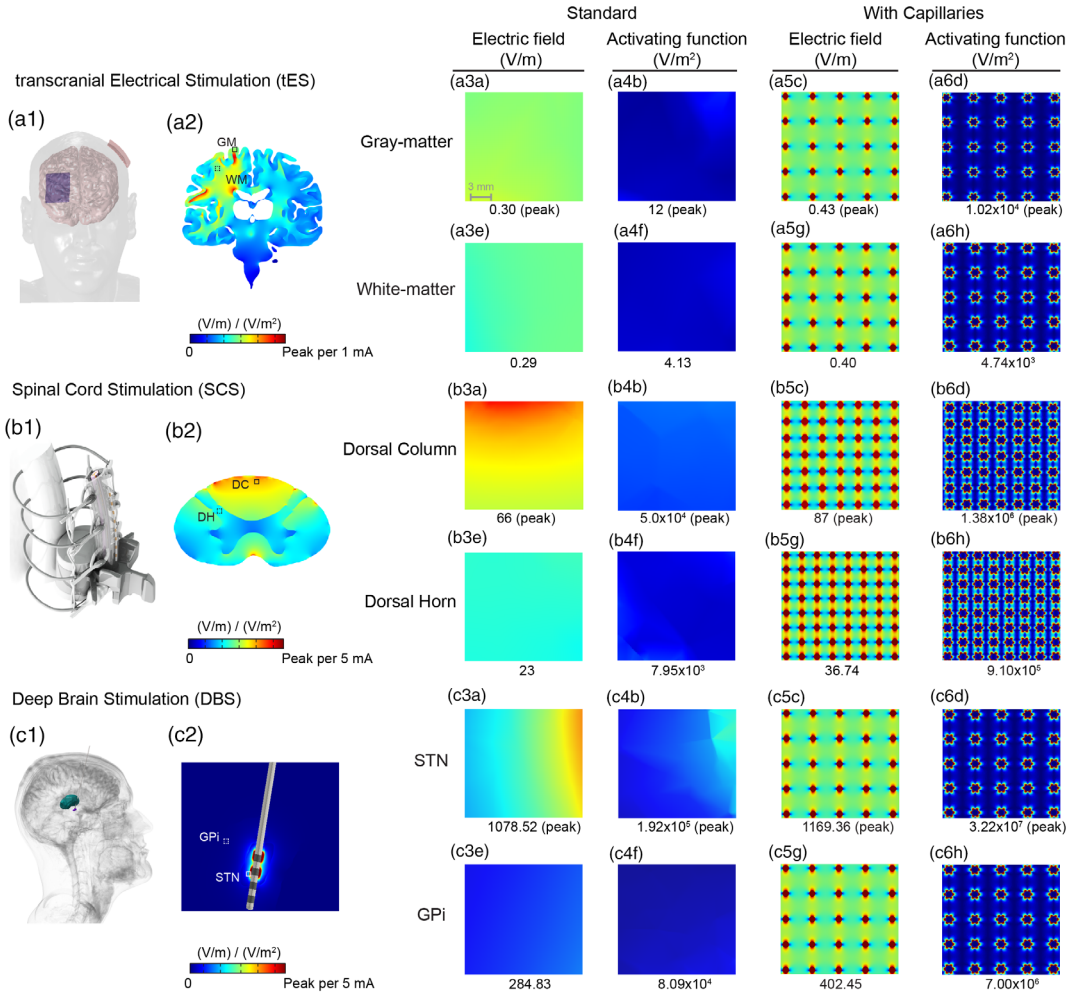

Figure 3. Application of neurocapillary-modulation in neuromodulation simulations of tES, DBS, and SCS. These exemplary simulations demonstrate the degree and spatial extent of electrical current flow distortion in the brain parenchyma around brain capillaries and the resulting amplification of neuronal polarization, driving factors such as electric field and activating function. a1. Conventional M1-SO tES montage predicts electric field distribution across the brain with a global pattern determined by macroscopic anatomy, as shown in a selected coronal slice (a2) under the M1 electrode. In a tES model without capillaries (standard model), (a3a, a3e) shows electric field distribution and (a4b, a4f) shows activating function within ROIs selected at the gray matter (GM) and white matter (WM). In a tES model with capillaries, there is a moderate increase in electric field (a5c, a5g) and a categorical increase in activating function (a6d, a6h). b1. A T8-T12 SCS model simulation with an eight-contact SCS lead positioned epidurally predicts electric field across the spinal cord based on macroscopic anatomy, as shown in a selected slice (b2), directly under an active electrode. In a model without capillaries represented, (b3a, b3e) shows electric field distribution and (b4b, b4f) shows activating function at ROIs defined at dorsal column (DC) and dorsal horn (DH). In a SCS model with capillaries represented, a moderately enhanced electric field (b5c, b5g) and a significantly elevated activating function (b6d, b6h) are predicted. c1. A model of a four-contact DBS lead positioned inside the subthalamic nucleus (STN) predicts a gross current flow pattern around the lead (c2), determined by the macroscopic properties. In a standard DBS model without capillaries represented, electric field distribution (c3a, c3e) and activating function (c4b, c4f) is predicted within ROIs selected at the STN and globus pallidus internus (GPi). In a DBS model with capillaries included, a moderately enhanced electric field (c5c, c5g) and a significantly enhanced activating function (c6d, c6h) is predicted. [Color figure can be viewed at wileyonlinelibrary.com]

with the objective of this section, we report local maxima for each stimulation. For example, peak E_{BBB} for the exemplary capillary morphologies I, II, and III (with standard r_{BBB}) were, per unit $\bar{E}_{BRAIN}$: 367 V/m per V/m at capillary bend, 443 V/m per V/m at capillary bend, and 617 V/m per V/m at capillary terminal, respectively (Fig. 1a3,b3,c3). We further predicted a varied electric field across the capillary wall thickness (i.e., the electric field changes across the BBB wall thickness). Unless otherwise stated, E_{BBB} is considered the average electric field across the capillary wall thickness for a given capillary segment, which is calculated using equation (3). In this section only, we also report the maximal "punctate" electric field across any point inside the capillary wall as E^*_{BBB}.

Based on cable theory (see Methods), we developed an analytical solution for maximum BBB polarization (V^A_{BBB}) which depends only on the space constant (λ_{BBB}) of the capillary (equation (7)). When V^A_{BBB} is expressed per unit $\bar{E}_{BRAIN}$, then the analytical maximum polarization length is simply λ_{BBB}. The analytical solution for maximum BBB electric field (E^A_{BBB}) is then:

$$E^A_{BBB} = \bar{E}_{BRAIN} \times \lambda_{BBB} / d_{th-BBB} \quad (11)$$

Thus, the analytical maximum electric field amplification factor is $\lambda_{BBB}/d_{th\text{-}BBB}$.

For all the numerically (FEM) simulated capillary parameter, we also predicted (Fig. 1e,d) the corresponding analytical maximal

BBB voltage (V^A_{BBB}) and electric field (E^A_{BBB}). λ_{BBB} depends on the square root of r_{BBB} (equation (8)), as a result, V^A_{BBB} and so E^A_{BBB}, vary by 10x across 100x changes in r_{BBB}. Note analytical predictions do not explicitly depend on capillary morphology (e.g., morphology 1, 2, or 3) but depend on BBB capillary wall and lumen properties. The I_1 and I_2 variations of capillary morphology 1 are thus the only models with different V^A_{BBB}. However, this difference is then absent for predicted E^A_{BBB} because of the additional dependence on $d_{th\text{-}BBB}$ (equation (11)).

In addition, across different variations of capillary morphologies and BBB capillary wall resistivities, we made two types of comparisons. First, for BBB polarization per unit parenchyma electric field, we compared numerical maxima (V_{BBB} per $\bar{E}_{BRAIN}$) with the analytical BBB polarization (V^A_{BBB} per $\bar{E}_{BRAIN}$) based on λ_{BBB} (Fig. 1, row d). Second, for the BBB electric field amplification (BBB electric field per unit parenchyma electric field) we compared numerically computed average (E_{BBB} per $\bar{E}_{BRAIN}$) and punctate (E^*_{BBB} per $\bar{E}_{BRAIN}$) BBB electric field amplification with the analytical BBB electric field amplification (E^A_{BBB} per $\bar{E}_{BRAIN}$) based on $\lambda_{BBB}/d_{th\text{-}BBB}$ (Fig. 1, row e).

Across all simulated conditions, the numerically computed maximum polarization length (V_{BBB} per $\bar{E}_{BRAIN}$) was less than the analytical maxima (λ_{BBB}). As a consequence, the numerically computed maximum average BBB electric field (E_{BBB} per $\bar{E}_{BRAIN}$) was also always less than the analytical maximum ($\lambda_{BBB}/d_{th\text{-}BBB}$). In some models, the within-wall numerical maximum BBB electric field (E^*_{BBB} per $\bar{E}_{BRAIN}$) exceed the analytical maximum but never by more than by a factor of two. Provided our assumptions, the analytical solution for maximum BBB polarization (equation (7)) and amplification factor (equation (10)) can thus be considered reasonable approximations.

Finally, note that for principle 1 analysis, an average ("bulk") $\bar{E}_{BRAIN}$ was assumed; however, distortion in electric field around the periphery of capillaries was already noted in these simulations and was central to the analysis of nonuniform E_{BRAIN} for principle 2.

Electric Fields Amplification at the BBB Across Neuromodulation Interventions (Principle 1)

We considered five exemplary brain stimulation techniques (tDCS, TMS, ECT, DBS, and SCS) with associated brain targets (cortical, white-matter, subcortical, thoracic spinal white-matter, and thoracic spinal gray-matter). For each brain region, capillary anatomy (wall thickness: $d_{th\text{-}BBB}$; capillary diameter: $2r_v$; lumen diameter: d_l), and BBB membrane and blood resistivities (r_{BBB} and r_{BLOOD}) were derived from prior literature (24–26, 68, 72, 73, 79–82). These values were used to calculate a representative BBB space constant (λ_{BBB}) for each brain region. Typical brain electric field produced by each stimulation modality was also derived from literature (60–67, 69–71). Finally, using the analytical method for predicting maximal BBB polarization length and BBB electric field amplification factor (Fig. 1), for each brain stimulation technique and associated brain region, the maximal BBB polarization (V_{BBB}) and BBB electric field (E_{BBB}) is predicted (Table 1).

The E^A_{BBB} ranges from ~100 V/m for tDCS of cortex to ~100 kV/m for DBS. We note that variations in dose within each neuromodulation modality (e.g., electrode separation) and which brain region is considered (e.g., distance from electrode) causes E_{BRAIN} to vary. Moreover, E_{BRAIN} (and so E_{BBB}) for any modality will vary linearly with applied current. Never-the-less, E^A_{BBB} is consistently greater by over two orders of magnitude than $\bar{E}_{BRAIN}$. The temporal waveform of E_{BBB} would vary for each modality and programming as these setting effect E_{BRAIN}. For example, E_{BBB} would be static for tDCS and would biophysically be pulse for other modalities. Our model assumes no temporal filtering (e.g., low pass) in the BBB amplification factor.

Theoretical Basis for Neuron Polarization Amplification by Capillary Ultrastructure (Principle 2)

We developed a theory to predict distortion of current flow in the brain parenchyma by capillary ultrastructure and implications for maximum neuronal polarization. For cortical, white matter, subcortical, thoracic spinal white matter, and thoracic spinal gray-matter, we derived capillary bed length density (L_v), surface density (S_v), volumetric density (V_v), numerical density (N_v), and intercapillary distance (ICD) (Table 2). A representative vascular network of parallel solid capillaries was modeled for each brain region (Fig. 2, column a). The model was designed to be independent of brain voxel dimension and provide a conservative (uniform, no tortuosity) capillary distribution (see Methods).

For each BBB geometry, the parenchyma electric field (E_{BRAIN}) and electric field gradient (Activating function) were calculated along three straight trajectories: Proximal (~5 μm away from a capillary at a nearest point), middle (centered between adjacent capillaries, half the inter-capillary distance at a nearest point), and distal (no capillary zone, ~100 μm from a capillary at a nearest point). E_{BRAIN} and activating function were reported (normalized to) per average parenchyma electric field ($\bar{E}_{BRAIN}$).

Electrical field in the brain parenchyma (E_{BRAIN}) was distorted around brain capillaries, producing ~50% modulation of the average parenchyma electric field ($\bar{E}_{BRAIN}$) (Fig. 2, columns b and c). This change occurs within less than half of an inter-capillary distance, producing activating functions of ~100 kV/m^2 per unit average parenchyma electric field ($\bar{E}_{BRAIN}$) (Fig. 2, column d). Both the depth of E_{BRAIN} modulation and spatial rate of change increased with capillary density.

Table 2. Capillary Network Parameters of Different Brain Region for Various Therapeutic Modes of Electrical Stimulation.

Brain regions	Therapeutic mode	Length density (L_v: mm/mm^3)	Surface density (S_v: mm^2/mm^3)	Volumetric density (V_v: mm^3/mm^3)	Numerical density (N_v: mm^{-3})	Intercapillary distance (ICD: μm) (83, 84)
Cortical	tDCS, TMS, ECT	256 (85)	7.9	0.02	492	45
White-matter	TMS, ECT, DBS	160 (86)	4.9	0.01	307	57
Subcortical	ECT, DBS	328 (52, 83, 87)	10.1	0.03	631	40
Thoracic white-matter	SCS	810 (88)	24.9	0.06	1558	25
Thoracic gray-matter	SCS	972 (88)	29.9	0.07	1869	23

Table 3. Electric Field Modulation and Activating Function Created by BBB Ultrastructure for Exemplary Neuromodulation Techniques and Brain Targets.

Brain region	Therapy mode	Average electric field in brain ROI $\bar{E}_{BRAIN}$ (V/m)	E_{BRAIN} modulation from capillary ultrastructure (V/m)	Neurocapillary activating function (from capillary ultrastructure) (V/m^2)	Conventional activating function (from macroscopic structure) (V/m^2)
Cortical	tDCS	0.27–0.3 (60, 61)	0.12–0.14	9.93×10^3–1.10×10^4	~0 (39, 89)
Cortical	TMS	56.5–157.7 (62–64)	25.4–70.9	2.08×10^6–5.80×10^6	~0 (63, 67)
Cortical	ECT	125–240 (63, 65, 66)	56.3–108	4.60×10^6–8.82×10^6	~0 (65, 90)
Subcortical	ECT	100–125 (65, 67)	42–52.5	3.35×10^6–4.19×10^6	~0 (65, 90)
STN, GPi, Thalamus	DBS	200–1069 (68–71)	60–320.7	6.70×10^6–3.58×10^7	~2×10^5 (71, 91)
White matter	SCS	14.7–60 (72, 73)	6.6–27	3.74×10^5–1.53×10^6	~5.0×10^4 (72, 77)
Gray matter	SCS	21 (72)	12.2	9.25×10^5	~8×10^3 (72, 77)

E_{BRAIN} modulation and activating functions are reported for the proximal neuronal trajectory.

Neuronal Stimulation Driven by Capillary Ultrastructure Across Neuromodulation Interventions (Principle 2)

We considered five exemplary brain stimulation techniques (tDCS, TMS, ECT, DBS, and SCS) with associated brain targets (cortical, white-matter, subcortical, thoracic spinal white-matter, and thoracic spinal gray-matter). For each region, relevant capillary anatomy (Table 2) was used to calculate modulated E_{BRAIN} (the range of E_{BRAIN} changes) and activating function per unit average parenchyma electric field ($\bar{E}_{BRAIN}$). Next, we combined these constants with specific brain electric fields (Table 3). This analysis assumes negligible "macroscopic" change in E_{BRAIN} across brain voxel in the absence of capillaries (i.e., the electric field is uniform for a homogenous brain voxel) such that any local changes in E_{BRAIN} and non-zero activating function are introduced by the presence of capillaries. However, it is the macroscopic changes that are conventionally assumed to drive neuronal stimulation for many modalities. We thus, contrasted activating functions generated by conventional macroscopic tissue changes (values derived from the literature (39, 63, 65, 67, 71, 72, 77, 89–92)) with the BBB ultrastructure generated activating function derived here. This comparison is subject to a range of assumptions (e.g., distance from electrodes) and simplifications (e.g., linear and homogenous capillary structure). Never-the-less, BBB ultrastructure driven changes may conservatively exceed those conventionally derived from macroscopic tissue changes (Table 3). Moreover, for some techniques, such as tDCS, the electric field is conventionally assumed uniform (39, 42) (zero activating function), but our analysis instead suggest that it is nonuniform because of spatial modulation by BBB ultrastructure.

Translational Applications of Neurocapillary-Modulation Principle 2

The application of neurocapillary-modulation principle 2, and further insight on its impact, was demonstrated for three neuromodulation technologies. tES applies weak current to the brain through electrode on the scalp, including tDCS and transcranial Alternating Current Stimulation (tACS), and with higher currents in electroconvulsive therapy (ECT) (93). In this case, we simulated the M1-SO montage with 1 mA applied current (Fig. 3a1); resulting brain electric fields (Fig. 3a2) were consistent with predictions from prior models (39, 60, 94), as governed by macroscopic anatomy (skin, skull, CSF, and brain). The electric fields in gray-matter and white-matter were largely uniform (Fig. 3a3a,e), reflected in minimal activating functions (Fig. 3a4b,f). Using a multiscale approach (see Methods), the average electric field in each ROI was applied to a brain voxel with region-specific capillary density. The resulting electric field was moderately elevated (Fig. 3a5c,g) compared to the capillary-absent (standard) case. The presence of capillaries resulted in a nonuniform electric field, reflected in a significantly elevated activation function (Fig. 3a6d,h). The conversion of a largely uniform electric field to a nonuniform may categorically impact neuromodulation.

Neurocapillary-modulation principle 2 was applied to an exemplary SCS model (Fig. 3b1) based on the RADO-SCS open-source model (72). Consistent with the prior models (77, 95–97), the macroscopic current flow patterns and the resultant electric fields were determined by a gross anatomy (Fig. 3b2). In a standard model without capillaries, electric field (Fig. 3b3a,e) and activating function (Fig. 3b4b,f) were predicted in the dorsal column and dorsal horn ROIs. The impact of capillaries was simulated by applying the average (incident) electric fields in each ROI to respective dorsal column or dorsal horn voxels with region-specific capillary density. Electric fields in the spinal cord increased moderately (Fig. 3b5c,g) while the activating functions increased significantly (~2 orders of magnitude) as a consequence of warping of current flow around capillaries (Fig. 3b6d,h).

Finally, we demonstrated the application of neurocapillary-modulation principle 2 to models of DBS. A model of STN targeted DBS (68, 98, 99) (Fig. 3c1) predicted current flow between energized leads (Fig. 3c2) based on macroscopic tissue properties. In a standard model without capillaries, the electric field (Fig. 3c3a,e) and activating function (Fig. 3c3b,c4f) in the STN and GPi ROIs were predicted. A multiscale models, where the average electric field in each ROI was applied to a brain voxel with region-specific capillary density, predicted a moderately elevated electric field (Fig. 3c5c,g) and a significantly elevated (~two orders of magnitude) activating function (Fig. 3c6d,h) across the ROI. Alongside stimulations of other neuromodulation technologies, this serves to illustrate that neurocapillary-modulation principle 2 acts at all distance from stimulating electrodes. Thus, while electrode configuration and macroscopic anatomy govern how much current (incident electric field) arrives at each ROI, the spatial profile of brain parenchyma electric field along the neurons depends on local capillary ultrastructure.

DISCUSSION

The study of which neural elements are activated by neuromodulation is exhaustive and includes verification in isolated systems without vasculature (100–102). The first principle of

neurocapillary-modulation, that primary stimulation of BBB function leads to secondary changes in neuronal activity, is complimentary to these conventional theories of direct neural stimulation. We predict that the maximal electric field across the BBB (E_{BBB}) is over two orders of magnitude above brain parenchyma (E_{BRAIN}), with a maximum amplification factor ($\lambda_{BBB}/d_{th\text{-}BBB}$) adapted from the cable theory. Electric field across the BBB modulate water and solute transport (20–22) which in turn regulate neuronal metabolic capacity and interstitial clearance. Brain imaging techniques that depend on hemodynamic changes are a bedrock of systems neuroscience (e.g., fMRI, fNIRS)—we suggest that in the specific case of neuromodulation, they can be interpreted as suggestive of direct capillary modulation (first principle) rather than secondary neurovascular coupling.

BBB integrity and NVC function is essential for the brain health and so cognition. Brain hemodynamics (NVC) and BBB transport are disrupted in aging (32, 33, 35, 103) and brain disease, including Alzheimer's disease and Parkinson's (104–106) and following brain injury (7, 107, 108). Indeed, BBB dysfunction may be a link across these disorders (109, 110). Notably, while Alzheimer's disease is traditionally considered a disease of neurofibrillary tangles and amyloid plaques, structural and functional changes in the microvessels may contribute directly to the pathogenesis of the disease (111–115), specifically disruption of brain clearance systems dependent on (water) transport across the BBB (30, 116, 117). For a wide range of brain disorders, there is interest in interventions modulating brain hemodynamics and clearance system; neuromodulation may have powerful and unique actions (principle 1).

When neuromodulation drives intense neuronal activity or relies on neuroplasticity, then neuromodulation is governed by brain metabolism and so by neurocapillary dynamics. The direct stimulation of the BBB by neuromodulation (principle 1) may thus also play a role in modulating metabolically active states created by direct neuronal stimulation mechanisms. To the extent, hemodynamic-based functional imaging of neuromodulation does not reflect direct BBB stimulation (principle 1) but rather conventional NVC, it still reinforces the role of the BBB in governing neuronal responses.

The second principle of neurocapillary-modulation address direct neural stimulation but with efficacy that is governed by current flow distortion around capillary ultrastructure. We develop a theory relating capillary density to local fluctuations in E_{BBB}. Stimulation of neurons is traditionally modeled as reflecting two cases: 1) changes in E_{BRAIN} along the neural structure (activating function (48, 118, 119)) and 2) polarization by locally uniform E_{BRAIN} (44, 59, 120). In the first case, E_{BRAIN} gradients are conventionally assumed to reflect macroscopic variation in both tissue resistivity and decay with distance from electrodes. However, by principle 2, local E_{BRAIN} gradients produced by BBB ultrastructure may overwhelm those changes driven by traditional macroscopic models (Table 3 and Fig. 3b,c). In the second case, principle 2 suggests locally uniform brain electric fields may in fact not exist (Table 3 and Fig. 3a). In both cases, that stimulation dose and macro-tissue properties still govern the ''incident'' E_{BRAIN} arriving at each brain target (modeled here as the average parenchyma electric field [$\bar{E}_{BRAIN}$]), which is then modulated by regional BBB ultrastructure (Fig. 3). In this sense, the quasi-uniform assumption remains valid (42, 43, 121). The tES, SCS, and DBS examples modeled here illustrate a multiscale implementation method applicable to any neuromodulation technology and suggest a high impact on resulting neuronal activation. However, the precise extent by which neurocapillary-modulation principle 2 reduces the threshold for stimulation, increases a spatial extent of neuromodulation, and alters which neuronal elements are activated will be application specific.

These neurocapillary-modulation principles are unrelated to BBB injury by electrical stimulation, which depends on electrochemical products (122, 123). Activation of neurogenic regulation of cardiac function (124–126) or brain clearance (127) including electrical stimulation of perivascular innervation (128) is distinct from the direct BBB polarization of principle 2. Electrical stimulation of glia (129–131) and subsequent astrocyte regulation of the BBB (132) are also parallel but distinct pathways.

The capillary bed of the brain is comprised of a tortuous network of intercommunicating vessels formed by specialized endothelial cells. Endothelial cells and pericytes are encased by basal lamina (~30–40 nm thick) containing collagen type IV, heparin sulfate proteoglycans, laminin, fibronectin, and other extracellular matrix proteins (133). The basal lamina of the brain endothelium is continuous with astrocytic end feet that ensheath the cerebral capillaries (134, 135). None of these details were modeled here and point to still more intricate mechanisms of neurocapillary-modulation. When considering larger vessels of the cerebrovascular tree, neurocapillary-modulation falls under the broader emerging field of neurovascular modulation—with broad applications in treatment of brain disease, especially disorders that are already linked to dysfunction in brain clearance or NVC.

Authorship Statements

Niranjan Khadka and Marom Bikson designed and prepared the manuscript with novel inputs. Niranjan Khadka ran the model, collected data, and analyzed the data. Marom Bikson edited and revised the manuscript. All authors approved the final manuscript.

How to Cite this Article:

Khadka N., Bikson M. 2020. Neurocapillary-Modulation. Neuromodulation 2020; E-pub ahead of print. DOI:10.1111/ner.13338

REFERENCES

1. Perlmutter JS, Mink JW, Bastian AJ et al. Blood flow responses to deep brain stimulation of thalamus. *Neurology* 2002;58:1388–1394.
2. Lang N, Siebner HR, Ward NS et al. How does transcranial DC stimulation of the primary motor cortex alter regional neuronal activity in the human brain? *Eur J Neurosci* 2005;22:495–504.
3. Zheng X, Alsop DC, Schlaug G. Effects of transcranial direct current stimulation (tDCS) on human regional cerebral blood flow. *NeuroImage* 2011;58:26–33.
4. Perrin JS, Merz S, Bennett DM et al. Electroconvulsive therapy reduces frontal cortical connectivity in severe depressive disorder. *Proc Natl Acad Sci U S A* 2012;109:5464–5468.
5. Ceballos-Baumann AO. Functional imaging in Parkinson's disease: activation studies with PET, fMRI and SPECT. *J Neurol* 2003;250:I15–I23.
6. Dougherty DD, Chou T, Corse AK et al. Acute deep brain stimulation changes in regional cerebral blood flow in obsessive-compulsive disorder. *J Neurosurgery* 2016;125:1087–1093.
7. Girouard H, Iadecola C. Neurovascular coupling in the normal brain and in hypertension, stroke, and Alzheimer disease. *J Appl Physiol (1985)* 2006;100:328–335.
8. Hosford PS, Gourine AV. What is the key mediator of the neurovascular coupling response? *Neurosci Biobehav Rev* 2019;96:174–181.

9. Hewson-Stoate N, Jones M, Martindale J, Berwick J, Mayhew J. Further nonlinearities in neurovascular coupling in rodent barrel cortex. *NeuroImage* 2005;24: 565–574.
10. Martin C, Martindale J, Berwick J, Mayhew J. Investigating neural–hemodynamic coupling and the hemodynamic response function in the awake rat. *NeuroImage* 2006;32:33–48.
11. Jones M, Hewson-Stoate N, Martindale J, Redgrave P, Mayhew J. Nonlinear coupling of neural activity and CBF in rodent barrel cortex. *NeuroImage* 2004;22: 956–965.
12. Logothetis NK, Pauls J, Augath M, Trinath T, Oeltermann A. Neurophysiological investigation of the basis of the fMRI signal. *Nature* 2001;412:150–157.
13. Cardoso MMB, Sirotin YB, Lima B, Glushenkova E, Das A. The neuroimaging signal is a linear sum of neurally distinct stimulus- and task-related components. *Nat Neurosci* 2012;15:1298–1306.
14. Lima B, Cardoso MMB, Sirotin YB, Das A. Stimulus-related neuroimaging in task-engaged subjects is best predicted by concurrent spiking. *J Neurosci* 2014;34: 13878–13891.
15. Nielsen AN, Lauritzen M. Coupling and uncoupling of activity-dependent increases of neuronal activity and blood flow in rat somatosensory cortex. *J Physiol.* 2001;533:773–785.
16. Ngai AC, Jolley MA, D'Ambrosio R, Meno JR, Winn HR. Frequency-dependent changes in cerebral blood flow and evoked potentials during somatosensory stimulation in the rat. *Brain Res* 1999;837:221–228.
17. Hoffmeyer HW, Enager P, Thomsen KJ, Lauritzen MJ. Nonlinear neurovascular coupling in rat sensory cortex by activation of transcallosal fibers. *J Cereb Blood Flow Metab* 2007;27:575–587.
18. Mathiesen C, Caesar K, Akgören N, Lauritzen M. Modification of activity-dependent increases of cerebral blood flow by excitatory synaptic activity and spikes in rat cerebellar cortex. *J. Physiol* 1998;512:555–566.
19. Akgören N, Dalgaard P, Lauritzen M. Cerebral blood flow increases evoked by electrical stimulation of rat cerebellar cortex: relation to excitatory synaptic activity and nitric oxide synthesis. *Brain Res* 1996;710:204–214.
20. Shin DW, Fan J, Luu E et al. In vivo modulation of the blood-brain barrier permeability by transcranial direct current stimulation (tDCS). *Ann Biomed Eng* 2020;48:1256–1270.
21. Cancel LM, Arias K, Bikson M, Tarbell JM. Direct current stimulation of endothelial monolayers induces a transient and reversible increase in transport due to the electroosmotic effect. *Sci Rep* 2018;8:9265.
22. Lopez-Quintero SV, Datta A, Amaya R, Elwassif M, Bikson M, Tarbell JM. DBS-relevant electric fields increase hydraulic conductivity of in vitro endothelial monolayers. *J Neural Eng* 2010;7:16005.
23. Pulgar VM. Direct electric stimulation to increase cerebrovascular function. *Front Syst Neurosci* 2015;9:1–5.
24. Duvernoy H, Delon S, Vannson JL. The vascularization of the human cerebellar cortex. *Brain Res Bull* 1983;11:419–480.
25. Nicholson C. Diffusion and related transport mechanisms in brain tissue. *Rep Prog Phys* 2001;64:815–884.
26. Schlageter KE, Molnar P, Lapin GD, Groothuis DR. Microvessel organization and structure in experimental brain tumors: microvessel populations with distinctive structural and functional properties. *Microvasc Res* 1999;58:312–328.
27. Wong AD, Ye M, Levy AF, Rothstein JD, Bergles DE, Searson PC. The blood-brain barrier: an engineering perspective. *Front Neuroeng* 2013;6:7.
28. Iliff JJ, Wang M, Liao Y et al. A paravascular pathway facilitates CSF flow through the brain parenchyma and the clearance of interstitial solutes, including amyloid β. *Sci Transl Med* 2012;4:147ra111.
29. Tarasoff-Conway JM, Carare RO, Osorio RS et al. Clearance systems in the brain-implications for Alzheimer disease. *Nat Rev Neurol* 2015;11:457–470.
30. Peng W, Achariyar TM, Li B et al. Suppression of glymphatic fluid transport in a mouse model of Alzheimer's disease. *Neurobiol Dis* 2016;93:215–225.
31. Kress BT, Iliff JJ, Xia M et al. Impairment of paravascular clearance pathways in the aging brain. *Ann Neurol.* 2014;76:845–861.
32. Lipecz A, Csipo T, Tarantini S et al. Age-related impairment of neurovascular coupling responses: a dynamic vessel analysis (DVA)-based approach to measure decreased flicker light stimulus-induced retinal arteriolar dilation in healthy older adults. *GeroScience* 2019;41:341–349.
33. Wiedenhoeft T, Tarantini S, Nyúl-Tóth Á et al. Fusogenic liposomes effectively deliver resveratrol to the cerebral microcirculation and improve endothelium-dependent neurovascular coupling responses in aged mice. *GeroScience* 2019; 41:711–725.
34. Xie L, Kang H, Xu Q et al. Sleep drives metabolite clearance from the adult brain. *Science* 2013;342:373–377.
35. Tarantini S, Yabluchanskiy A, Csipo T et al. Treatment with the poly(ADP-ribose) polymerase inhibitor PJ-34 improves cerebromicrovascular endothelial function, neurovascular coupling responses and cognitive performance in aged mice, supporting the NAD+ depletion hypothesis of neurovascular aging. *GeroScience* 2019;41:533–542.
36. McIntyre CC, Grill WM, Sherman DL, Thakor NV. Cellular effects of deep brain stimulation: model-based analysis of activation and inhibition. *J Neurophysiol.* 2004;91:1457–1469.
37. Ye H, Steiger A. Neuron matters: electric activation of neuronal tissue is dependent on the interaction between the neuron and the electric field. *J Neuroeng Rehabil* 2015;12:65.
38. McIntyre CC, Grill WM. Excitation of central nervous system neurons by non-uniform electric fields. *Biophys J* 1999;76:878–888.
39. Datta A, Bansal V, Diaz J, Patel J, Reato D, Bikson M. Gyri-precise head model of transcranial direct current stimulation: improved spatial focality using a ring electrode versus conventional rectangular pad. *Brain Stimul* 2009;2:201–207.e1.
40. Rattay F. The basic mechanism for the electrical stimulation of the nervous system. *Neuroscience* 1999;89:335–346.
41. Holsheimer J. Computer modelling of spinal cord stimulation and its contribution to therapeutic efficacy. *Spinal Cord* 1998;36:531–540.
42. Bikson M, Truong DQ, Mourdoukoutas AP et al. Modeling sequence and quasi-uniform assumption in computational neurostimulation. *Prog Brain Res* 2015; 222:1–23.
43. Khadka N, Truong DQ, Williams P, Martin JH, Bikson M. The quasi-uniform assumption for spinal cord stimulation translational research. *J Neurosci Methods* 2019;328:108446.
44. Arlotti M, Rahman A, Minhas P, Bikson M. Axon terminal polarization induced by weak uniform DC electric fields: a modeling study. *Annu Int Conf IEEE Eng Med Biol Soc* 2012;2012:4575–4578.
45. Rahman A, Lafon B, Bikson M. Multilevel computational models for predicting the cellular effects of noninvasive brain stimulation. *Prog Brain Res* 2015;222: 25–40.
46. Rahman A, Reato D, Arlotti M et al. Cellular effects of acute direct current stimulation: aomatic and synaptic terminal effects. *J Physiol* 2013;591:2563–2578.
47. McNeal DR. Analysis of a model for excitation of myelinated nerve. *IEEE Trans Biomed Eng* 1976;23:329–337.
48. Rattay F. Analysis of models for external stimulation of axons. *IEEE Trans Biomed Eng* 1986;33:974–977.
49. Cassot F, Lauwers F, Fouard C, Prohaska S, Lauwers-Cances V. A novel three-dimensional computer-assisted method for a quantitative study of microvascular networks of the human cerebral cortex. *Microcirculation* 2006;13:1–18.
50. Zawiliński J, Litwin JA, Nowogrodzka-Zagórska M, Gorczyca J, Miodoński AJ. Vascular system of the human spinal cord in the prenatal period: a dye injection and corrosion casting study. *Ann Anat Anat Anz* 2001;183:331–340.
51. Mozumder M, Pozo JM, Coelho S et al. Quantitative histomorphometry of capillary microstructure in deep white matter. *NeuroImage Clin* 2019;23:1–8.
52. Kreczmanski P, Heinsen H, Mantua V et al. Microvessel length density, total length, and length per neuron in five subcortical regions in schizophrenia. *Acta Neuropathol* 2009;117:409–421.
53. Pienaar IS, Lee CH, Elson JL et al. Deep-brain stimulation associates with improved microvascular integrity in the subthalamic nucleus in Parkinson's disease. *Neurobiol Dis.* 2015;74:392–405.
54. Bouras C, Kövari E, Herrmann FR et al. Stereologic analysis of microvascular morphology in the elderly: Alzheimer disease pathology and cognitive status. *J Neuropathol Exp Neurol* 2006;65:235–244.
55. Marín-Padilla M. The human brain intracerebral microvascular system: development and structure. *Front Neuroanat* 2012;6:38.
56. Lauwers F, Cassot F, Lauwers-Cances V, Puwanarajah P, Duvernoy H. Morphometry of the human cerebral cortex microcirculation: general characteristics and space-related profiles. *NeuroImage* 2008;39:936–948.
57. Rubinstein JT. Axon termination conditions for electrical stimulation. *IEEE Trans. Biomed Eng* 1993;40:654–663.
58. Chakraborty D, Truong DQ, Bikson M, Kaphzan H. Neuromodulation of axon terminals. *Cereb Cortex N Y N* 2018;28:2786–2794.
59. Tranchina D, Nicholson C. A model for the polarization of neurons by extrinsically applied electric fields. *Biophys J.* 1986;50:1139–1156.
60. Truong DQ, Magerowski G, Blackburn GL, Bikson M, Alonso-Alonso M. Computational modeling of transcranial direct current stimulation (tDCS) in obesity: impact of head fat and dose guidelines. *NeuroImage Clin* 2013;2:759–766.
61. Datta A, Truong D, Minhas P, Parra LC, Bikson M. Inter-individual variation during transcranial direct current stimulation and normalization of dose using MRI-derived computational models. *Front Psychiatry* 2012;3:91.
62. Janssen AM, Oostendorp TF, Stegeman DF. The coil orientation dependency of the electric field induced by TMS for M1 and other brain areas. *J NeuroEng Rehabil* 2015;12:47.
63. Deng Z-D, Liston C, Gunning FM et al. Electric field modeling for transcranial magnetic stimulation and electroconvulsive therapy. In: Makarov S, Horner M, Noetscher G, editors. *Brain and human body modeling: computational human modeling at EMBC 2018*. Cham: Springer International Publishing, 2019; p. 75–84.
64. Mikkonen M, Laakso I, Sumiya M, Koyama S, Hirata A, Tanaka S. TMS motor thresholds correlate with TDCS electric field strengths in Hand motor area. *Front Neurosci.* 2018;12:426.
65. Bai S, Gálvez V, Dokos S, Martin D, Bikson M, Loo C. Computational models of bitemporal, bifrontal and right unilateral ECT predict differential stimulation of brain regions associated with efficacy and cognitive side effects. *Eur Psychiatr* 2017;41:21–29.
66. Argyelan M, Oltedal L, Deng Z-D et al. Electric field causes volumetric changes in the human brain. *eLife* 2019;8:1–20.
67. Lee WH, Lisanby SH, Laine AF, Peterchev AV. Comparison of electric field strength and spatial distribution of electroconvulsive therapy and magnetic seizure therapy in a realistic human head model. *Eur Psychiatry* 2016;36:55–64.
68. Khadka N, Harmsen IE, Lozano AM, Bikson M. Bio-heat model of kilohertz-frequency deep brain stimulation increases brain tissue temperature. *Neuromodulation Technol* 2020;23:489–495.
69. Hemm S, Mennessier G, Vayssiere N, Cif L, Fertit HE, Coubes P. Deep brain stimulation in movement disorders: Stereotactic coregistration of two-dimensional

electrical field modeling and magnetic resonance imaging. *J Neurosurgery* 2005; 103:949–955.
70. Hemm S, Mennessier G, Vayssière N, Cif L, Coubes P. Co-registration of stereotactic MRI and isofieldlines during deep brain stimulation. *Brain Res Bull* 2005; 68:59–61.
71. Astrom M, Diczfalusy E, Martens H, Wardell K. Relationship between neural activation and electric field distribution during deep brain stimulation. *IEEE Trans Biomed Eng* 2015;62:664–672.
72. Khadka N, Liu X, Zander H et al. Realistic anatomically detailed open-source spinal cord stimulation (RADO-SCS) model. *J Neural Eng* 2020;17:1–12.
73. Hernández-Labrado GR, Polo JL, López-Dolado E, Collazos-Castro JE. Spinal cord direct current stimulation: Finite element analysis of the electric field and current density. *Med Biol Eng Comput* 2011;49:417–429.
74. Leite J, Gonçalves ÓF, Pereira P et al. The differential effects of unihemispheric and bihemispheric tDCS over the inferior frontal gyrus on proactive control. *Neurosci Res* 2018;130:39–46.
75. Seibt O, Truong D, Khadka N, Huang Y, Bikson M. Computational finite element method (FEM) forward modeling workflow for transcranial direct current stimulation (tDCS) current flow on MRI-derived head: simpleware and COMSOL Multiphysics tutorial. *bioRxiv* 2019;704940. https://doi.org/10.1101/704940.
76. Alam M, Truong DQ, Khadka N, Bikson M. Spatial and polarity precision of concentric high-definition transcranial direct current stimulation (HD-tDCS). *Phys Med Biol* 2016;61:4506–4521.
77. Zannou AL, Khadka N, Truong DQ et al. Temperature increases by kilohertz frequency spinal cord stimulation. *Brain Stimul* 2019;12:62–72.
78. Zannou AL, Khadka N, FallahRad M, Truong DQ, Kopell BH, Bikson M. Tissue temperature increases by a 10 kHz spinal cord stimulation system: phantom and bioheat model. *Neuromodulation* 2019. https://doi.org/10.1111/ner.12980.
79. Hasgall PA, Di Gennaro F, Baumgartner C, et al. IT'IS Database for thermal and electromagnetic parameters of biological tissues. Version 4.0. May 15, 2018. https://doi.org/10.13099/VIP21000-04-0.
80. Butt AM, Jones HC, Abbott NJ. Electrical resistance across the blood-brain barrier in anaesthetized rats: a developmental study. *J Physiol* 1990;429:47–62.
81. Srinivasan B, Kolli AR, Esch MB, Abaci HE, Shuler ML, Hickman JJ. TEER measurement techniques for in vitro barrier model systems. *J Lab Autom* 2015;20: 107–126.
82. Marquez J, van Vliet P, McElduff P, Lagopoulos J, Parsons M. Transcranial direct current stimulation (tDCS): does it have merit in stroke rehabilitation? A systematic review. *Int J Stroke* 2015;10:306–316.
83. Boero JA, Ascher J, Arregui A, Rovainen C, Woolsey TA. Increased brain capillaries in chronic hypoxia. *J Appl Physiol (1985)* 1999;86:1211–1219.
84. Dockery P, Fraher J. The quantification of vascular beds: a stereological approach. *Exp Mol Pathol* 2007;82:110–120.
85. Kubíková T, Kochová P, Tomášek P, Witter K, Tonar Z. Numerical and length densities of microvessels in the human brain: correlation with preferential orientation of microvessels in the cerebral cortex, subcortical grey matter and white matter, pons and cerebellum. *J Chem Neuroanat* 2018;88:22–32.
86. Kaplan S. Non-steroidal anti-inflammatory drugs and nervous system development. *J Chem Neuroanat* 2018;87:1.
87. Acer N, Bastepe-Gray S, Sagiroglu A et al. Diffusion tensor and volumetric magnetic resonance imaging findings in the brains of professional musicians. *J Chem Neuroanat* 2018;88:33–40.
88. O'Sullivan C, Dockery P, Fraher JP. P2: The vascular anatomy of the human spinal cord. *J Anat* 2004;205:528.
89. Jiang J, Truong DQ, Esmaeilpour Z, Huang Y, Badran BW, Bikson M. Enhanced tES and tDCS computational models by meninges emulation. *J Neural Eng* 2020;17:016027.
90. Deng Z-D, Lisanby SH, Peterchev AV. Electric field strength and focality in electroconvulsive therapy and magnetic seizure therapy: a finite element simulation study. *J Neural Eng* 2011;8:016007.
91. Kuncel AM, Cooper SE, Grill WM. A method to estimate the spatial extent of activation in thalamic deep brain stimulation. *Clin Neurophysiol* 2008;119: 2148–2158.
92. Deng Z-D, Lisanby SH, Peterchev AV. Controlling stimulation strength and focality in electroconvulsive therapy via current amplitude and electrode size and spacing: comparison with magnetic seizure therapy. *J ECT* 2013;29: 325–335.
93. Bikson M, Esmaeilpour Z, Adair D et al. Transcranial electrical stimulation nomenclature. *Brain Stimul* 2019;12:1349–1366.
94. Khadka N, Truong DQ, Bikson M. Principles of within electrode current steering. *J Med Devices* 2015;9:020947-020947–2.
95. Lempka SF, McIntyre CC, Kilgore KL, Machado AG. Computational analysis of kilohertz frequency spinal cord stimulation for chronic pain management *J. Am Soc Anesthesiol* 2015;122:1362–1376.
96. Zhang TC, Janik JJ, Grill WM. Modeling effects of spinal cord stimulation on wide-dynamic range dorsal horn neurons: influence of stimulation frequency and GABAergic inhibition. *J Neurophysiol.* 2014;112:552–567.
97. Arle JE, Carlson KW, Mei L, Iftimia N, Shils JL. Mechanism of dorsal column stimulation to treat neuropathic but not nociceptive pain: analysis with a computational model. *Neuromodulation* 2014;17:642–655. discussion 655.
98. Miocinovic S, Lempka SF, Russo GS et al. Experimental and theoretical characterization of the voltage distribution generated by deep brain stimulation. *Exp. Neurol* 2009;216:166–176.
99. Baniasadi M, Proverbio D, Gonçalves J, Hertel F, Husch A. FastField: an open-source toolbox for efficient approximation of deep brain stimulation electric fields. *NeuroImage* 2020;223:117330.
100. Maccabee PJ, Amassian VE, Eberle LP, Cracco RQ. Magnetic coil stimulation of straight and bent amphibian and mammalian peripheral nerve in vitro: locus of excitation. *J Physiol.* 1993;460:201–219.
101. Bikson M, Inoue M, Akiyama H et al. Effects of uniform extracellular DC electric fields on excitability in rat hippocampal slices in vitro. *J Physiol* 2004;557: 175–190.
102. Förstl J, Galvan M, ten Bruggencate G. Extracellular K+ concentration during electrical stimulation of rat isolated sympathetic ganglia, vagus and optic nerves. *Neuroscience* 1982;7:3221–3229.
103. Csipo T, Mukli P, Lipecz A et al. Assessment of age-related decline of neurovascular coupling responses by functional near-infrared spectroscopy (fNIRS) in humans. *GeroScience* 2019;41:495–509.
104. Grammas P, Martinez J, Miller B. Cerebral microvascular endothelium and the pathogenesis of neurodegenerative diseases. *Expert Rev. Mol Med* 2011; 13:e19.
105. Sweeney MD, Sagare AP, Zlokovic BV. Blood-brain barrier breakdown in Alzheimer disease and other neurodegenerative disorders. *Nat Rev Neurol* 2018; 14:133–150.
106. Amtul Z, Yang J, Lee T-Y, Cechetto DF. Pathological changes in microvascular morphology, density, size and responses following comorbid cerebral injury. *Front Aging Neurosci* 2019;11:47.
107. Jang H, Huang S, Hammer DX et al. Alterations in neurovascular coupling following acute traumatic brain injury. *Neurophotonics* 2017;4:045007.
108. Wright AD, Smirl JD, Bryk K, van Donkelaar P. A prospective transcranial Doppler ultrasound-based evaluation of the acute and cumulative effects of sport-related concussion on neurovascular coupling response dynamics. *J Neurotrauma* 2017;34:3097–3106.
109. Rosengarten B, Dannhardt V, Burr O et al. Neurovascular coupling in Parkinson's disease patients: effects of dementia and acetylcholinesterase inhibitor treatment. *J Alzheimers Dis* 2010;22:415–421.
110. Abrahamson EE, Ikonomovic MD. Brain injury-induced dysfunction of the blood brain barrier as a risk for dementia. *Exp Neurol* 2020;328:113257.
111. Drachman DA. The amyloid hypothesis, time to move on: Amyloid is the downstream result, not cause, of Alzheimer's disease. *Alzheimers Dement* 2014;10: 372–380.
112. Tarantini S, Tran CHT, Gordon GR, Ungvari Z, Csiszar A. Impaired neurovascular coupling in aging and Alzheimer's disease: Contribution of astrocyte dysfunction and endothelial impairment to cognitive decline. *Exp Gerontol* 2017;94: 52–58.
113. Liu Y, Braidy N, Poljak A, Chan DKY, Sachdev P. Cerebral small vessel disease and the risk of Alzheimer's disease: a systematic review. *Ageing Res. Rev* 2018; 47:41–48.
114. Costea L, Mészáros Á, Bauer H et al. The blood-brain barrier and its intercellular junctions in age-related brain disorders. *Int J Mol Sci* 2019;20:1–28.
115. Roquet D, Sourty M, Botzung A, Armspach J-P, Blanc F. Brain perfusion in dementia with Lewy bodies and Alzheimer's disease: an arterial spin labeling MRI study on prodromal and mild dementia stages. *Alzheimers Res Ther* 2016; 8:29.
116. Anderson VC, Lenar DP, Quinn JF, Rooney WD. The blood-brain barrier and microvascular water exchange in Alzheimer's disease. *Cardiovasc Psychiatry Neurol* 2011;2011:615829.
117. van de Haar HJ, Burgmans S, Jansen JFA et al. Blood-brain barrier leakage in patients with early Alzheimer disease. *Radiology* 2016;281:527–535.
118. Warman EN, Grill WM, Durand D. Modeling the effects of electric fields on nerve fibers: determination of excitation thresholds. *IEEE Trans Biomed Eng* 1992;39: 1244–1254.
119. McIntyre CC, Grill WM. Extracellular stimulation of central neurons: influence of stimulus waveform and frequency on neuronal output. *J Neurophysiol* 2002;88: 1592–1604.
120. Radman T, Ramos RL, Brumberg JC, Bikson M. Role of cortical cell type and morphology in subthreshold and suprathreshold uniform electric field stimulation in vitro. *Brain Stimul* 2009;2:215–228.e1-3.
121. Bikson M, Dmochowski J, Rahman A. The "quasi-uniform" assumption in animal and computational models of non-invasive electrical stimulation. *Brain Stimulat* 2013;6:704–705.
122. Pudenz RH, Bullara LA, Jacques S, Hambrecht FT. Electrical stimulation of the brain. III. The neural damage model. *Surg. Neurol* 1975;4:389–400.
123. Fox JL, Yasargil MG. The experimental effect of direct electrical current on intracranial arteries and the blood-brain barrier. *J Neurosurgery* 1974;41: 582–589.
124. ter Laan M, van Dijk JMC, Stewart R, Staal MJ, Elting J-W. Modulation of cerebral blood flow with transcutaneous electrical neurostimulation (TENS) in patients with cerebral vasospasm after subarachnoid hemorrhage. *Neuromodulation* 2014;17:431–436. discussion 436-437.
125. ter Laan M, van Dijk JMC, Elting JWJ, Staal MJ, Absalom AR. Sympathetic regulation of cerebral blood flow in humans: a review. *Br J Anaesth* 2013;111: 361–367.
126. Bapna A, Adin C, Engelman ZJ, Fudim M. Increasing blood pressure by greater splanchnic nerve stimulation: a feasibility study. *J Cardiovasc Transl Res* 2019;13: 509–518.

127. Cheng K, Brodnick SK, Blanz SL et al. Clinically-derived vagus nerve stimulation enhances cerebrospinal fluid penetrance. *Brain Stimulat* 2020;13: 1024–1030.
128. Suzuki N, Hardebo JE. The cerebrovascular parasympathetic innervation. *Cerebrovasc Brain Metab Rev* 1993;5:33–46.
129. Bikson M, Lian J, Hahn PJ, Stacey WC, Sciortino C, Durand DM. Suppression of epileptiform activity by high frequency sinusoidal fields in rat hippocampal slices. *J Physiol* 2001;531:181–191.
130. Vallejo R, Platt DC, Rink JA et al. Electrical stimulation of C6 glia-precursor cells in vitro differentially modulates gene expression related to chronic pain pathways. *Brain Sci* 2019;9:1–13.
131. Monai H, Ohkura M, Tanaka M et al. Calcium imaging reveals glial involvement in transcranial direct current stimulation-induced plasticity in mouse brain. *Nat Commun* 2016;7:11100.
132. MacVicar BA, Newman EA. Astrocyte regulation of blood flow in the brain. *Cold Spring Harb Perspect Biol* 2015;7:1–14.
133. Thomsen MS, Routhe LJ, Moos T. The vascular basement membrane in the healthy and pathological brain. *J Cereb Blood Flow Metab* 2017;37:3300–3317.
134. Daneman R, Prat A. The blood-brain barrier. *Cold Spring Harb Perspect Biol* 2015; 7:a020412.
135. Jessen NA, Munk ASF, Lundgaard I, Nedergaard M. The Glymphatic system: a Beginner's guide. *Neurochem Res* 2015;40:2583–2599.

